

Programmable Nanoarchitectonics of Pore Array for Electronic-Nose-Based Early Disease Diagnose

Xiaofang Pan¹, Xiaojin Zhao¹, Senior Member, IEEE, Wei Xu¹,
Zhiyong Fan, Senior Member, IEEE, and Amine Bermak²

Abstract—In this article, we present a novel electronic nose fabrication process based on highly programmable anodic aluminum oxide (AAO) nanoarchitectonics and ultrasonic spray pyrolysis (USP) deposition. Featuring an ultralow manufacturing cost, the deposited material's morphology can be accurately controlled with fabricated general-purpose AAO template. Compared with nonstandard lithography-based template fabrication method, the need of complicated Bosch etching process and its associated complex process parameter tuning is eliminated. As a result, the cost-effective mass production of 3-D nanotemplate-based material and devices can be enabled. In addition, the target material's limited coverage and time efficiency issues widely existing in the previous deposition methods are well-addressed by our customized USP deposition, especially for the 3-D nanotemplate with large surface-to-volume ratio, leading to significantly improved gas-sensing performance. Moreover, the proposed fabrication recipe, together with the adopted gas recognition algorithms based on linear discriminant analysis (LDA), is validated based on the reported extensive measurement results for five gas biomarkers widely exploited for patients' exhaled gas-sensing and recognition applications. This shows great potential for the early disease diagnose of diabetes, breast cancer, acute lung injury, colon diseases, lung cancer, and so on.

Manuscript received 7 January 2022; revised 8 April 2022 and 5 May 2022; accepted 24 May 2022. Date of publication 10 June 2022; date of current version 25 July 2022. This work was supported in part by the National Natural Science Foundation of China under Grant 62174111; in part by the Guangdong Basis and Applied Basic Research Foundation under Grant 2021A1515011488; in part by the Shenzhen-Hong Kong Joint Innovation Foundation under Grant SGDX20190919094401725; in part by the Fundamental Research Foundation of Shenzhen under Grant JCYJ20190808151819049; and in part by the Open Foundation of the State Key Laboratory of Digital Manufacturing Equipment and Technology under Grant DMETKF2021016. The review of this article was arranged by Editor N. Donato. (Corresponding author: Xiaojin Zhao.)

Xiaofang Pan and Xiaojin Zhao are with the College of Electronics and Information Engineering, Shenzhen University, Shenzhen 518060, Guangdong, China (e-mail: eexjzhao@szu.edu.cn).

Wei Xu is with the College of Electronics and Information Engineering, Shenzhen University, Shenzhen 518060, China, and also with the State Key Laboratory of Digital Manufacturing Equipment and Technology (DMET), Huazhong University of Science and Technology, Wuhan 430074, China.

Zhiyong Fan is with the Department of ECE, Hong Kong University of Science and Technology, Clear Water Bay, Hong Kong, China.

Amine Bermak is with the College of Science and Engineering, Hamad Bin Khalifa University, Education City, Doha, Qatar.

Color versions of one or more figures in this article are available at <https://doi.org/10.1109/TED.2022.3178364>.

Digital Object Identifier 10.1109/TED.2022.3178364

Index Terms—Disease diagnose, high-aspect-ratio material deposition, machine learning classification algorithm, programmable template fabrication, sensor synthesis.

I. INTRODUCTION

OVER the past decades, a typical nanoarchitectonics [1], pore array, has attracted extensive research attention due to its intriguing chemical/physical characteristics, such as high surface to volume ratio, ultracompact size [2], low cost [3], easy fabrication [4], and simplicity of operation [5]. Demonstrated applications include gas sensor [6], [7], biosensor [8], [9], photonic sensor [10], heavy metal sensor [11], solar cell [12], and supercapacitor [13], to name a few. Attributed to their active interactions between the gas molecules and the interfaces, pore array-based gas sensors can exhibit ultrahigh sensitivity within short response time [14], [15]. More importantly, based on a sensor array integrating various types of gas sensors with diverse sensitivities to a target gas species, the sensors' response signals are largely different, which can form specific signal patterns that are recognizable using advanced classification algorithms [16], [17]. This array-based gas-sensing and recognizing system, which is also known as “electronic nose,” has become a promising noninvasive approach for the early diagnosis of a wide range of diseases, according to the gas biomarkers in the patients' exhaled breath [18].

In order to fabricate nanoporous devices with high performance, template-based process flow takes great advantage in terms of accurate morphology control [19], and there are typically two main steps involved for the previous implementations [20]: template fabrication and material deposition. Specifically, photolithography is adopted for patterning nanoscale template. However, it does not perform well for 3-D nanotemplate with high aspect ratio and periodic pitch in the range of 1–2 μm [21]. As a result, dedicated displacement Talbot lithography with Bosch etching process is needed to achieve accurate control of the 3-D morphology of the template. In addition, hard mask and extra process steps are necessary for the abovementioned nonstandard lithography and etching process, where the process parameters of gas flow, pressure, and RF power must be carefully tuned [21].

Regarding the other main step, material deposition, several methods have been applied to uniformly covering the interior

surface deep inside the designed 3-D nanotemplate, such as electrodeposition [22]–[24], chemical bath deposition [25], spin coating [26], sputtering [27], [28], and atomic layer deposition (ALD) [29]. Among them, ALD is more advantageous due to its exhibited higher accuracy and controllability of the target material’s morphology and thickness. However, for nanotemplate with large surface-to-volume ratio and high aspect ratio, there are two major drawbacks for ALD-based deposition.

- 1) *The Need of Consuming Large Amount of Relatively Expensive Precursor Material With Significantly Increased Pressure and Dosing Time* [20], [29]: It is known that the coverage of precursor material over the whole nanoporous structure is crucial to the following target material’s deposition. Because of the high aspect ratio, both the pressure and the dosing time need to be greatly increased for maximizing the aforesaid coverage, leading to large consumption of the precursor material.
- 2) *Poor Deposition Time Efficiency*: In [29], it is reported that up to 15 days are required to deposit the target material with a thickness of 480 nm onto the surface of the adopted nanotube-based template.

In order to address the above issues, in this article, we propose an ultralow-cost and highly programmable and scalable methodology for fabricating a general-purpose 3-D anodic aluminum oxide (AAO) nanoporous template. In addition, we further demonstrate an ultrasonic spray pyrolysis (USP)-based process, to deposit a thin layer of gas-sensing SnO₂ film and form the designed electronic nose. Compared with previously reported implementations, the AAO-based 3-D nanoporous template features much larger surface area, which can significantly improve the adsorption and reaction of target gas species. More importantly, the proposed program-controlled automatic fabrication approach enables a cost-effective way for mass production of 3-D nanotemplate-based material and devices with superior stability and repeatability [30], [31]. Moreover, the proposed USP-based material deposition well addresses the target material’s coverage and time efficiency issues widely existing in the previous methods, especially for 3-D nanotemplate with sophisticated interior topologies [32]. With the optimized recipe combining the aforesaid AAO template and USP-based deposition, we can have 3-D nanopore array-based electronic nose fabricated with excellent gas-sensing performance. This is validated by our reported extensive experimental results with five gas biomarkers of nitrogen dioxide, formaldehyde, methane, acetone, and isopropyl alcohol (IPA), which are widely exploited in the exhaled gas-sensing and recognition applications for early disease diagnose. Consequently, all the gas biomarkers can be well-recognized with the fabricated electronic nose prototype using the mainstream linear discriminant analysis (LDA).

II. MATERIALS AND METHODS

A. Design of Highly Programmable Nanoporous Templates

Fig. 1 shows the proposed gas sensor structure with its detailed fabrication process. First, a nanoporous template with target depth from 10 to 80 μm is fabricated through a

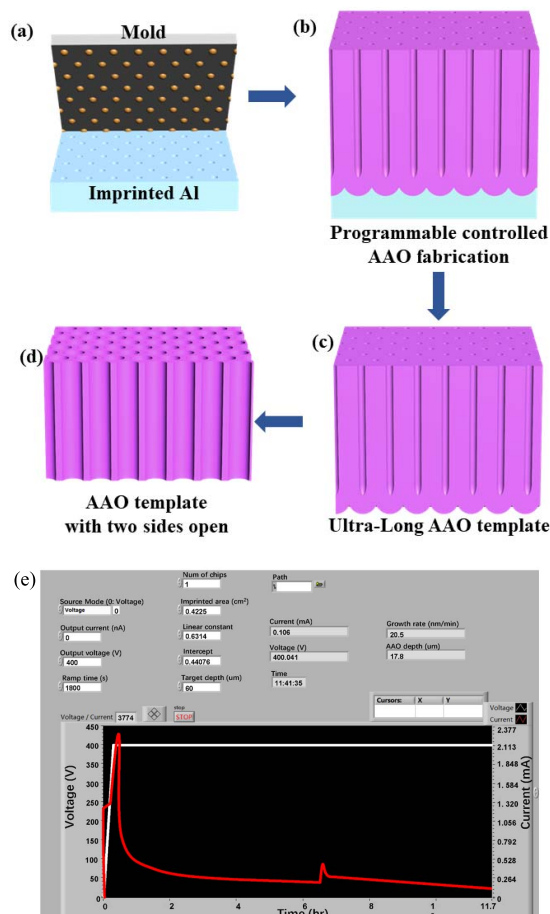


Fig. 1. Proposed fabrication schematic of 3-D nanoporous template. (a) Al foil is imprinted by hexagonally ordered pillar array silicon mold. (b) Perfectly ordered nanopore array with high aspect ratio is grown under the program control. (c) Al substrate layer at the bottom of the template is removed. (d) Bottom of AAO is dissolved and the tube of AAO is widened. (e) Screenshot of the autofabrication software with real-time current/voltage/growth depth monitoring.

program-controlled anodization procedure, which is largely different from traditional manual manipulations requiring rich experience, especially for the dynamic optimization of the acid concentration and growing temperature. As shown in Fig. 1(a), a clean and polished Al foil is imprinted by our prefabricated silicon mold (hexagonally ordered pillar array). After this “printing process,” the predesigned pattern with 1- μm period is transferred onto the surface of Al to initiate the growth of highly ordered AAO. Afterward, Al is anodized to AAO using mixed solution of citric acid, ethylene glycol, and phosphoric acid [see Fig. 1(b)].

Due to the linear correlation between the nanopore depth and the integrated charge density during the electrochemical anodization process, a customized fabrication control system incorporating Keithley 2400 source meter is exploited to provide a large range of anodization voltage from 0 to 400 V. Meanwhile, it is capable of recording the anodization current, precisely monitoring the AAO growth, initiating the replenishment of phosphoric acid, and automatically terminating the anodization when the target nanopore depth is achieved. In order to further visualize the growing process, a user-friendly GUI based on LabVIEW is developed and its interface is shown in Fig. 1(e). With this homemade GUI, we can input

the growth condition and monitor the real-time parameters of anodization and the target nanopore depth. Specifically, as presented in Fig. 1(e) in the left upper part of the software, there are a few empirical parameters for AAO's growth, such as the anodization voltage ($V_{\text{anod}} = D_{\text{int}}(\text{nm})/2.5$ (nm) V, D_{int} is the interpore distances), the ramping time for this high anodization voltage (short ramping time leads to overheating of the electrolyte, while long ramping time results in a fairly flat AAO film without the designed structure), the number of chips to be anodized (up to 12), the imprinted area, and the slope/intercept of the linear fitting curve between AAO depth and anodization current density. In the right upper part, the GUI with real-time parameters, including anodization currents, anodization voltage, and AAO depth, are illustrated. In the middle of the software interface, a vivid real-time I - V curve of the anodization voltage and current is presented. It is observed that the anodization current increases instantaneously with the voltage rising up to 400 V. With the aluminum oxide growing on the surface of AAO nanopore template, the concentration of phosphoric acid and the anodization current gradually decreases.

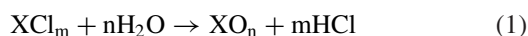
After a long time, the current density is decreased to a low level, leading to a very slow growth of the AAO. In order to maintain the growth rate, the phosphoric acid is added to the anodization solution with a volume step of 2 mL. As a result, both the current and growth rate are recorded to increase sharply [after 6 h in Fig. 1(e)]. By using this customized smart system, we can fabricate the designed AAO template with ultralong depth, which corresponds to ultrahigh aspect ratio.

Afterward, the Al substrate layer at the bottom of the template is removed by immersing it into the HgCl solution [see Fig. 1(c)]. Successively, 5% phosphoric acid is used to dissolve the bottom of AAO and widen the tube of AAO as well [see Fig. 1(d)]. Finally, a bundle of symmetrical nanopores with two open sides is formed.

B. Conformal SnO₂ Deposition Through High-Aspect-Ratio AAO

By using the fabricated AAO nanopores with depth from 10 to 80 μm , SnO₂ film can be uniformly deposited using a novel USP method featuring low cost, high aspect ratio, and large surface area. This simple and efficient USP setup is shown in Fig. 2(a), consisting of an atomization unit in the left part and a decomposition part in the right. For atomization, a piezoelectric vibrator is installed at the bottom of the water container, which transfers the vibration to the precursor solution through water, making the solution atomized. Compressed air is then injected into the precursor solution container, which delivers precursor mist to the top surface of the hotplate. At the decomposing part of the precursor solution, the sample is placed under the spray nozzle with the top and bottom surfaces facing the spray nozzle subsequently, as shown in Fig. 2(b.1) and (b.2).

The detailed reaction in the decomposition zone depends on the surface hydrolysis of metal chloride on hotplate according to the following chemical reaction equation:



where X represents the metal of Sn, Zn, or Cu.

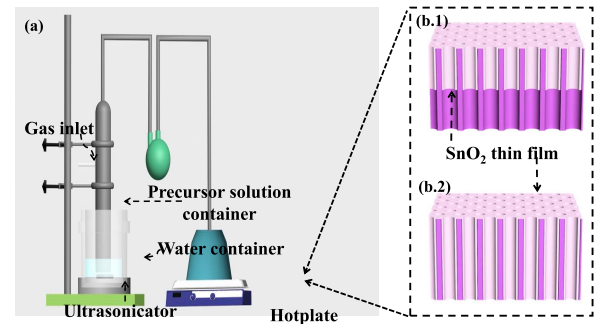


Fig. 2. (a) Illustrated USP deposition facility with the left part of the ultrasonic vibrator as the atomization unit and the right part of the hotplate as the decomposition part. (b) Fabricated nanoporous templates are placed under the spray nozzle with the top and bottom surfaces facing the spray nozzle subsequently.

C. Material Characterization

The microstructure and detailed material distribution of the sensor fabricated following the proposed procedure are checked using scanning electron microscopy (SEM; JEOL Ltd.; JSM-6700 F) and the energy-dispersive X-ray spectroscopy (EDS; JEOL Ltd.; JSM-6700 F). The crystal phase of the SnO₂ material is characterized by the X-ray diffraction (XRD, CuK α).

D. Measurement of Gas Sensors

The gas-sensing performance characterization setup consists of four mass flow controllers (MKS) and one intelligent gas sensing and analysis system. The target biomarker is ordered through Dalian Special Gases Company Ltd., with expected concentration diluted in dry air (CH₂O: 4 ppm; IPA: 6000 ppm; methane: 4000 ppm; acetone: 5 ppm; and NO₂: 25 ppm). During the experiment, mass flow controllers (MFCs) are used to monitor the volume of the gas biomarkers injected into the chamber of CGS-4TPS system. By keeping the airflow velocity stable (500 sccm in total), the concentration of the biomarker is adjusted by changing the ratio between the dry air and the target biomarker. Then, the CGS-4TPS system is used to acquire the real-time resistance through the customized data board. The fabricated samples to be tested are placed in the center of the chamber of the CGS-4TPS system with probes connected and a heater under the substrate. During the test, the sensors are heated up to 200 $^{\circ}\text{C}$ and stepped concentrations of biomarkers are sequentially injected with a period of 20 min to ensure the full response of the sensors followed with 30 min of dry air to ensure the full recovery of the sensors.

III. RESULTS AND DISCUSSION

A. Material Characterization and Analysis

By precisely controlling the substrate temperature, this novel, simple and cost-effective method is successfully demonstrated, and a highly conformal SnO₂ is coated over these high-aspect-ratio AAO templates without the shadow effect. As shown in Fig. 3, samples are deposited with temperatures rising from 250 $^{\circ}\text{C}$ to 380 $^{\circ}\text{C}$ by a step of ~ 50 $^{\circ}\text{C}$. Below 350 $^{\circ}\text{C}$, SnO₂ is hard to be deposited on AAO surface, as shown in Fig. 3(a) and (b). When the temperature is elevated to 350 $^{\circ}\text{C}$, SnO₂ becomes crystallized with a thickness of ~ 76 nm in 4 min [see Fig. 3(c)].

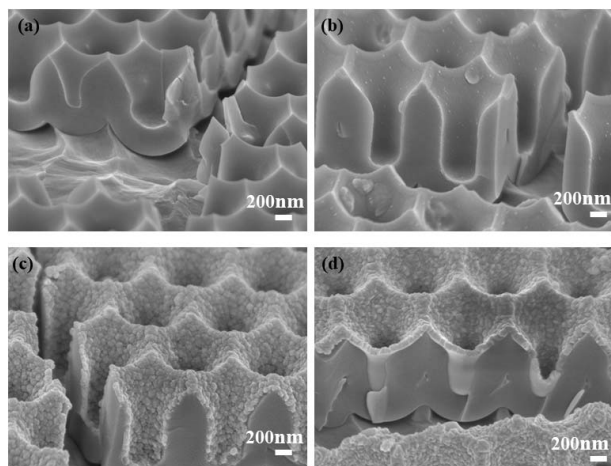


Fig. 3. (a) SEM picture of SnO₂ deposited at 250 °C for 8 min. (b) SEM picture of SnO₂ deposited at 300 °C for 8 min. (c) SEM picture of SnO₂ deposited at 350 °C for 4 min. (d) SEM picture of SnO₂ deposited at 380 °C for 4 min.

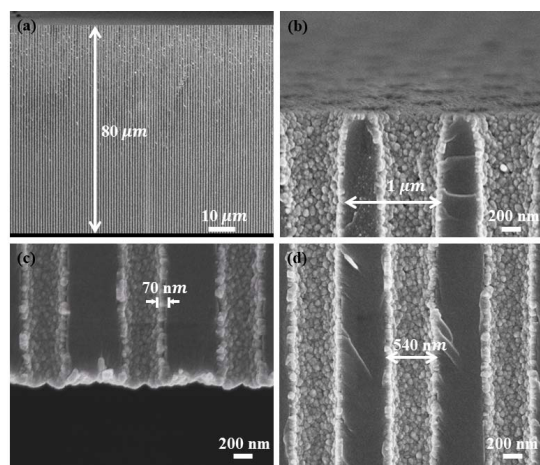


Fig. 4. (a) SEM picture of SnO₂ deposited in 80- μ m nanoporous AAO template. (b) Zoomed picture for the top part. (c) Zoomed picture for the bottom part. (d) Zoomed picture for the middle part.

By further increasing the temperature up to 380 °C, the morphology of SnO₂ can be well-preserved with a higher deposition rate. As a result, eventual thickness of the deposited films in 4 min is measured to be 80 nm [see Fig. 3(d)]. In Fig. 4, we present the scanning results of the SnO₂ film based on a typical 80- μ m AAO template. It is observed that highly ordered and dense AAO nanoporous template is covered by a uniform thin film of SnO₂ [see Fig. 4(a)]. Zoomed images of top [see Fig. 4(b)], bottom [see Fig. 4(c)], and middle parts [see Fig. 4(d)] of AAO template further validate that the crystallized SnO₂ film is uniformly deposited on the sidewall of 1- μ m period template with AAO nanopore's diameter equal to \sim 540 nm.

Besides the intrinsic USP deposition mechanism, the AAO nanoporous structure with two open sides also contributes to this satisfactory deposition with high step coverage. Concretely, the pressure inside the AAO nanopore template is significantly decreased due to the opened bottom, which leads to deep penetration of the SnO₂ spray and large sensing surface to the target gas. Meanwhile, the adopted dual depositions at both bottom and top surfaces (see Fig. 4) can further

TABLE I
COMPARISON WITH OTHER DEPOSITION METHODS
OF 3-D NANOPOROUS TEMPLATES

Deposition Method	Material	Aspect ratio	Uniformity	Time	References
Electrodeposition	Cu	Not mentioned	All filled, not uniform	1-3 seconds	[22]
	Pb	4.5	All filled ¹	60 seconds	[23]
	Cu ₂ O	8.25	Not uniform	Not mentioned	[24]
Chemical bath deposition	CdTe quantum dots	87	Good	> 2 hours	[25]
Spin coating	Amorphous As ₂ S ₇	120	Good ²	> 10 hours	[26]
Sputtering	Pt	2.5	Only top surface	Not mentioned	[27]
	Au/Pt/Pd/Polystyrene	2.5	Good	Not mentioned	[28]
Atomic layer deposition	Ir	180	Good	15 days	[29]
Our proposed method	SnO ₂	148	Good	80 minutes	

¹ Annealing is needed to make it hollow.

² One side is all filled.

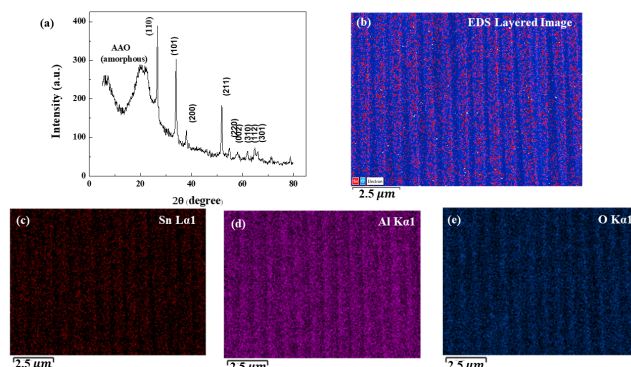


Fig. 5. (a) XRD pattern of SnO₂ film deposited on AAO template. (b)–(e) Material components distribution of SnO₂ deposited nanoporous template characterized by EDS.

dramatically improve the poor step coverage of SnO₂ reported in previous studies, including electrodeposition [22]–[24] and sputtering [27], [28]. As listed in Table I, electrodeposition and sputtering are only suitable for templates with relatively low aspect ratio. Although uniform coating for high-aspect-ratio nanoarchitectonics can be achieved through the chemical bath deposition, its applications are limited to the deposition of only several kinds of quantum dots [25], [33]. In addition, spin coating can exhibit superior deposition results compared with the abovementioned deposition methods [26]. Nevertheless, the deposited material fully fills all the tubes of the template, which prevents the gas molecules from penetrating into the whole template. What is more, the processing time needed for spin coating is reported to be as long as 10 h. Regarding the atomic layer deposition method [29], an aspect ratio as high as 180 can be achieved. However, it is at the expense of extremely high fabrication cost and long deposition time up to 15 days.

Crystal structures of nanoparticles synthesized at 380 °C are examined by XRD and are shown in Fig. 5(a), which reveals that the SnO₂ particles with tetragonal rutile lattice structure (JCPDS 41-1445) are present. XRD reflections at 2θ values of 26.6°, 34.0°, 38.0°, 51.9°, 54.75°, 64.82°, 65.93°, and 61.7° correspond to the (110), (101), (200), (211), (220), (112), and (301) planes, respectively. The broad diffraction peak at 20.44° is due to AAO because SnO₂ nanoparticles are deposited on

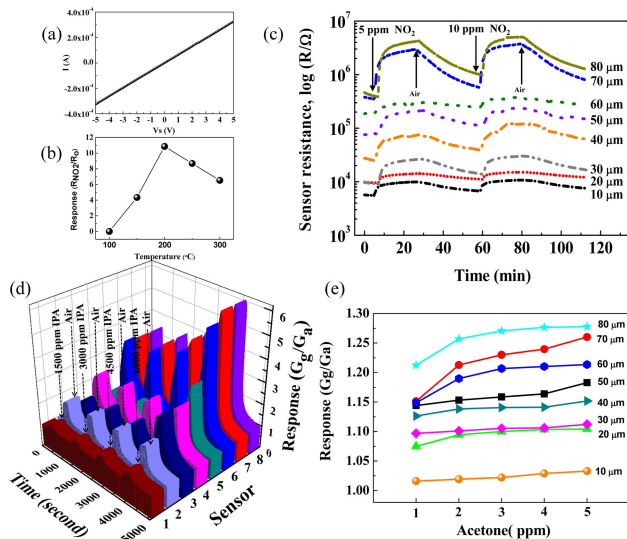


Fig. 6. (a) I - V of the sensor with 30- μm nanoporous AAO template. (b) Response of 80- μm AAO template-based gas sensor for 5-ppm NO_2 at different temperatures. (c) Time-domain responses of the sensor array to 5- and 10-ppm NO_2 in dry air at 200 °C. (d) Time-domain performances of the sensor array for 1500–6000-ppm IPA at 200 °C. (e) Responses of all eight sensors (based on 10–80- μm nanoporous templates) for 1–5-ppm acetone.

AAO, together with SEM images confirming the deposition of SnO_2 into this high-aspect-ratio nanotemplate.

Besides, according to the cross-sectional images of EDS presented in Fig. 5(b)–(e), the deposited SnO_2 's excellent uniformity is well-validated.

B. Characterization of the Electronic and Gas-Sensing Property

I - V of the sensor with 30- μm -depth AAO template is presented in Fig. 6(a). It is clear that the contact is ohmic. After the electronic property characterization, to get the optimum working temperature, the sensor is tested at a step of 50 °C from 100 °C to 300 °C [see Fig. 6(b)]. It turns out that the peak response is acquired at 200 °C for 5 ppm NO_2 . Therefore, the operating temperature is set as 200 °C for all eight sensors. For the sensing test, the sensor array is characterized using different gases widely adopted as the biomarkers of various diseases, as shown in Table II (see [34]–[40]).

Fig. 6(c) and (d) shows the measured sensing performance of our fabricated sensor array for these different gas biomarkers. First, Fig. 6(c) shows the transient responses to 5- and 10-ppm NO_2 in dry air at 200 °C. The baseline resistance of the sensor array increases as the depths of the nanoarchitectonics increased from 10 to 80 μm . Because when the current flows between two electrodes on the diagonal, the average length of the current path increases with deeper nanoarchitectonics, leading to larger resistance in series. When sequential 5- and 10-ppm NO_2 flow into the reaction chamber, the resistance of sensors increases. When NO_2 is stopped and air begins flowing into the chamber, the resistance recovers. According to the sensing mechanism, the sensor resistance change is caused by the strong reaction between the NO_2 molecule (typical oxidizing gas) and the surface states of SnO_2 material. During this

TABLE II
SOME BIOMARKERS OF THE EXHALED BREATH
AND THE CORRESPONDING DISEASES

Biomarker	Acetone	Formaldehyde	Nitrogen Dioxide	IPA	Methane
Disease	Diabetes	Breast cancer	Acute lung injury	Lung cancer	Colonic fermentation, colon cancer

process, free electrons are captured by the surface adsorbed NO_2 molecules and the surface depletion region is expanded leading to an increased resistance. Besides, comparing the dynamic response of different sensors, there is an obvious trend that sensors based on deeper nanoarchitectonics have a larger resistance change after exposure to NO_2 molecules.

The real-time gas-sensing performance of IPA is also shown in Fig. 6(d). It is observed that the conductance increases with the gas injection, which is caused by the reduction reaction between IPA and O_x^- ions. It is known that, in the air, oxygen molecules are adsorbed at the oxygen vacancy site of the SMO material's surface, and O_x^- ions formed with trapped electrons lead to a decrease of the electron density. During the gas reaction process, the above trapped electrons are released freely into the conduction band and the conductance is increased consequently. Specifically, high sensitivity, fast response (the average response/recovery time equal to 14 and 475 s), and stable sensing response are observed for IPA with the concentration varying from 1500 to 6000 ppm at 200 °C. For another biomarker gas of acetone, the response is plotted in Fig. 6(e). Meanwhile, it is observed that the sensor with longer AAO (e.g., 80 μm) features a larger surface area and exhibits more dramatic response change. As the dipole moment of acetone (2.88) is higher compared with IPA (1.58), CH_2O (2.33), and methane (0), acetone was more easily adsorbed and activated, thus further promoting the oxidation reaction with oxygen species on the surface of SnO_2 .

It is obvious that using the resistance ratio between the baseline resistance (R_a) and saturation resistance (R_g) is hard to clearly separate acetone, methane, and formaldehyde [see Fig. 7(a)]. Based on the above measurement results, LDA is applied to visualize and enhance the discrimination effect of the proposed gas-sensing system. LDA is a widely adopted machine learning method for multidimensional feature vector reduction and linear classification. This method allows one to transfer the multidimensional sensor signals related to different analytes into an artificial multidimensional feature space where the linear combination of features provides the best separation of the tested analytes [41]. To achieve this goal, the main mathematical step is to find a feature space where the within-class variance is the smallest and the between-class variance is the largest. After R_a/R_g of each sensor as the input projected onto the first two or three linear discriminants in this feature space, the distribution and the separability of all gas sample data can be visualized in Fig. 7(b), where it is indicated that all kinds of gases are clearly separated, and the biomarker gases are well distinguished. Specifically, IPA and nitrogen dioxide are most distanced from all the other analytes, corresponding to the situation of the selectivity figure with acetone, methane, and formaldehyde closer. However, from the LDA figure, it is

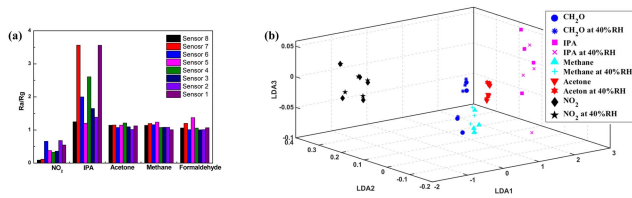


Fig. 7. (a) Selectivity test result: the R_a/R_g value of the sensor array for 5-ppm NO₂, 1500-ppm IPA, 5-ppm acetone, 1000-ppm methane, and 4-ppm formaldehyde. (b) Classification result based on the LDA algorithm of our proposed electronic nose system for CH₂O (1–4 ppm), IPA (1500–6000 ppm), methane (1000–4000 ppm), acetone (1–5 ppm), and NO₂ (5–25 ppm) under both dry condition and 40% RH.

clear that acetone, methane, and formaldehyde are separable with the machine learning algorithm.

To explore the influence of humidity, we tested the analytes at 40% RH. The classification result is shown in Fig. 7(a) and it is clear that the projected sample dots are little deviated from the original samples tested in the dry air, whereas with eight sensors, different analytes are still separable in the projected feature space.

IV. CONCLUSION

In this article, we have demonstrated a cost-effective recipe for fabricating gas-sensor-array-based electronic nose system, which is based on highly programmable AAO nanoporous template and USP deposition with superior coverage of the gas-sensing material SnO₂. Compared with previous implementations, the fabrication cost and time can be significantly reduced. Attributed to the proposed 3-D nanoporous template featuring ultralarge surface-to-volume ratio, the fabricated gas sensor array exhibits superior sensing performance when exposed to five widely adopted gas biomarkers. With the customized LDA dimension reduction method, the proposed implementation is suitable for a wide range of diseases' early diagnose based on the patients' exhaled breath.

APPENDIX

A. GUI

The GUI is developed by LABVIEW software to control and monitor Keithley 2400 source and meter unit, which provides the anodization voltage of the template process. In the upper left part of GUI, we can first select the source mode (voltage or current) and input the corresponding output amplitude, such as output voltage or output current. Then, an empirical ramp time for the Keithley 2400 unit to reach the output voltage is set. Then, in the second column, the number of chips that can be simultaneously fabricated is inputted, followed with the imprinted area that is imprinted by the mold. It is reported that there is a linear correlation between AAO pore depth and integrated charge density [1]; therefore, the linear constant and intercept obtained by fitting the above relationship is input. By recording real-time current, timely calculating the integrated charge density and corresponding AAO pore depth, once the inputted target depth is reached, the anodization will be terminated. Then, the measured parameters of the fabrication process are shown in the right part, such as current, voltage, and time. Besides, the calculated growth rate and the AAO depth are demonstrated. The detailed mechanism

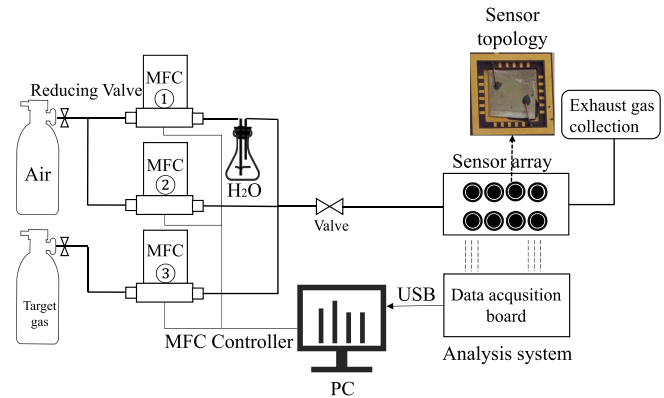


Fig. 8. Schematic of the electronic nose testing system.

between the AAO depth (or growth rate) and the anodization condition is provided in [42].

In the bottom part, the real-time situation of current (red line) and the voltage is visually presented to give the operator a vivid view of the whole fabrication process. As shown in Fig. 1(e), the anodization voltage reaches 400 V after 1800 s and keeps stable. During the process, the current increases sharply with the voltage and decreases gradually since the concentration of phosphoric acid is reduced. In order to maintain a satisfactory growth rate, the phosphoric acid is added at interval to increase the anodization current and growth rate.

B. Schematics of the Testing Setup

The electrodes are pasted at the diagonal side of the sensor array using high-temperature carbon paste. Eight sensors are placed in a 700-mL reaction chamber. As shown in Fig. 8, the mass flow controller (MFC) helps control the speed of the gases flowing into the reaction chamber, and target concentrations of gases are acquired by changing the ratio between different channels of MFC. In addition, dry air or target gas with humidity can be acquired by controlling the switch of the MFC in channel 1. The MFC helps control the speed of the gases flowing into the reaction chamber, and target concentrations of gases are acquired by changing the ratio between different channels of MFC. In addition, we can simulate the exhaled gases of real situations with 40% RH. The signal acquisition board of the electronic nose system is fabricated by Beijing Elite Technology Company Ltd.

C. Machine Learning Part of the Electronic Nose System

For LDA processing, we take R_g/R_a of each sensor as the input, where R_g is the saturation resistance with target gas and R_a is the baseline resistance at air. As we take pure air as the background, we did not demonstrate it in Fig. 7. With eight sensors in the array, we can see that biomarkers are clearly separated.

The Mahalanobis distance of an observation \vec{x} from a set of observations with mean $\vec{\mu}$ and covariance matrix S is defined as

$$D_M(\vec{x}) = \sqrt{(\vec{x} - \vec{\mu})^T S^{-1} (\vec{x} - \vec{\mu})}$$

The Mahalanobis distance is a measure of the distance between a point P and a distribution D , introduced by P. C. Mahalanobis in 1936. It is a multidimensional

generalization of the idea of measuring how many standard deviations away P is from the mean of D . This distance is zero if P is at the mean of D and grows as P moves away from the mean along each principal component axis. Here, the input of the Mahalanobis is the eigenvectors.

REFERENCES

- [1] K. Ariga, "Nanoarchitectonics: What's coming next after nanotechnology?" *Nanosc. Horizons*, vol. 6, no. 5, pp. 364–378, 2021.
- [2] N. Taşaltın, S. Öztürk, N. Kiliç, and Z. Z. Öztürk, "Temperature dependence of a nanoporous Pd film hydrogen sensor based on an AAO template on Si," *Appl. Phys. A, Solids Surf.*, vol. 97, no. 4, p. 745, 2009.
- [3] Y. Guo, S. Gao, W. Yue, C. Zhang, and Y. Li, "AAO-assisted low-cost flexible capacitive pressure sensors based on double-sided nanopillars by facile fabrication method," *ACS Appl. Mater. Interfaces*, vol. 11, no. 51, pp. 48594–48603, 2019.
- [4] A. K. Kasi, J. K. Kasi, and M. Bokhari, "Fabrication of mechanically stable AAO membrane with improved fluid permeation properties," *Microelectron. Eng.*, vols. 187–188, pp. 95–100, Feb. 2018.
- [5] H. Robatjazi, S. M. Bahaeddin, L. H. Macfarlan, S. Fu, and I. Thomann, "Ultrathin AAO membrane as a generic template for sub-100 nm nanostructure fabrication," *Chem. Mater.*, vol. 28, no. 13, pp. 4546–4553, Jul. 2016.
- [6] J.-H. Jeun and S.-H. Hong, "CuO-loaded nano-porous SnO₂ films fabricated by anodic oxidation and RIE process and their gas sensing properties," *Sens. Actuators B, Chem.*, vol. 151, no. 1, pp. 1–7, Nov. 2010.
- [7] T. Hyodo, E. Fujii, K. Ishida, T. Ueda, and Y. Shimizu, "Microstructural control of porous In₂O₃ powders prepared by ultrasonic-spray pyrolysis employing self-synthesized polymethylmethacrylate microspheres as a template and their NO₂-sensing properties," *Sens. Actuators B, Chem.*, vol. 244, pp. 992–1003, Jun. 2017.
- [8] M. A. Tabrizi, J. Ferre-Borrull, and L. F. Marsal, "Remote sensing of Salmonella-specific DNA fragment by using nanoporous alumina modified with the single-strand DNA probe," *Sens. Actuators B, Chem.*, vol. 304, Feb. 2020, Art. no. 127302.
- [9] G. Rajeev, E. Xifre-Perez, B. P. Simon, A. J. Cowin, L. F. Marsal, and N. H. Voelcker, "A label-free optical biosensor based on nanoporous anodic alumina for tumour necrosis factor- α detection in chronic wounds," *Sens. Actuators B, Chem.*, vol. 257, pp. 116–123, Mar. 2018.
- [10] W.-T. Tsai, M.-H. Nguyen, J.-R. Lai, H.-B. Nguyen, M.-C. Lee, and F.-G. Tseng, "ppb-level heavy metal ion detection by electrochemistry-assisted nanoPorous silicon (ECA-NPS) photonic sensors," *Sens. Actuators B, Chem.*, vol. 265, pp. 75–83, Jul. 2018.
- [11] M.-O. Park, K.-D. Seo, Y.-B. Shim, J.-H. Yoon, and D.-S. Park, "Chromium(VI) sensor based on catalytic reduction using the nanoporous layer of poly(aminopyrimidyl-terthiophene) and AuNi composite," *Sens. Actuators B, Chem.*, vol. 301, Dec. 2019, Art. no. 127151.
- [12] S.-F. Leung *et al.*, "Efficient photon capturing with ordered three-dimensional nanowell arrays," *Nano Lett.*, vol. 12, no. 7, pp. 3682–3689, Jul. 2012.
- [13] Q. Wei, Y. Fu, G. Zhang, D. Yang, G. Meng, and S. Sun, "Rational design of novel nanostructured arrays based on porous AAO templates for electrochemical energy storage and conversion," *Nano Energy*, vol. 55, pp. 234–259, Jan. 2019.
- [14] Z. Zhao, T. M. Dansereau, M. A. Petrukhhina, and M. A. Carpenter, "Nanopore-array-dispersed semiconductor quantum dots as nanosensors for gas detection," *Appl. Phys. Lett.*, vol. 97, no. 11, Sep. 2010, Art. no. 113105.
- [15] F. Rumiche, H. H. Wang, W. S. Hu, J. E. Indacochea, and M. L. Wang, "Anodized aluminum oxide (AAO) nanowell sensors for hydrogen detection," *Sens. Actuators B, Chem.*, vol. 134, no. 2, pp. 869–877, Sep. 2008.
- [16] J. W. Gardner and P. N. Bartlett, "A brief history of electronic noses," *Sens. Actuators B, Chem.*, vol. 18, nos. 1–3, pp. 210–211, 1994.
- [17] B. Liu, X. Wu, K. W. L. Kam, W.-F. Cheung, and B. Zheng, "Cuprous oxide based chemiresistive electronic nose for discrimination of volatile organic compounds," *ACS Sensors*, vol. 4, no. 11, pp. 3051–3055, Nov. 2019.
- [18] G. Peng *et al.*, "Diagnosing lung cancer in exhaled breath using gold nanoparticles," *Nature Nanotechnol.*, vol. 4, no. 10, pp. 669–673, 2009.
- [19] Q. Lin, S.-F. Leung, K.-H. Tsui, B. Hua, and Z. Fan, "Programmable nanoengineering templates for fabrication of three-dimensional nanophotonic structures," *Nanosc. Res. Lett.*, vol. 8, no. 1, p. 268, Dec. 2013.
- [20] R. Zazpe *et al.*, "Atomic layer deposition for coating of high aspect ratio TiO₂ nanotube layers," *Langmuir*, vol. 32, no. 41, pp. 10551–10558, Oct. 2016.
- [21] K. Jefimovs *et al.*, "High-aspect ratio silicon structures by displacement Talbot lithography and Bosch etching," *Proc. SPIE*, vol. 10146, Mar. 2017, Art. no. 101460L.
- [22] J. M. Macak, B. G. Gong, M. Hueppe, and P. Schmuki, "Filling of TiO₂ nanotubes by self-doping and electrodeposition," *Adv. Mater.*, vol. 19, no. 19, pp. 3027–3031, Oct. 2007.
- [23] J. M. Macak *et al.*, "Ordered ferroelectric lead titanate nanocellular structure by conversion of anodic TiO₂ nanotubes," *Adv. Mater.*, vol. 21, no. 30, pp. 3121–3125, Aug. 2009.
- [24] L. Assaud, V. Heresanu, M. Hanbücken, and L. Santinacci, "Fabrication of p/n heterojunctions by electrochemical deposition of Cu₂O onto TiO₂ nanotubes," *Comp. Rendus Chimie*, vol. 16, no. 1, pp. 89–95, Jan. 2013.
- [25] X.-F. Gao, H.-B. Li, W.-T. Sun, Q. Chen, F.-Q. Tang, and L.-M. Peng, "CdTe quantum dots-sensitized TiO₂ nanotube array photoelectrodes," *J. Phys. Chem. C*, vol. 113, no. 18, pp. 7531–7535, May 2009.
- [26] J. M. Macak, T. Kohoutek, L. Wang, and R. Beranek, "Fast and robust infiltration of functional material inside titania nanotube layers: Case study of a chalcogenide glass sensitizer," *Nanoscale*, vol. 5, no. 20, pp. 9541–9545, 2013.
- [27] N. T. Nguyen, J. Yoo, M. Altomare, and P. Schmuki, "Suspended Pt nanoparticles over TiO₂ nanotubes for enhanced photocatalytic H₂ evolution," *Chemical Commun.*, vol. 50, no. 68, pp. 9653–9656, 2014.
- [28] J. Yoo, K. Lee, and P. Schmuki, "Templating using self-aligned TiO₂ nanotube stumps: Highly ordered metal and polymer bumped arrays," *ChemElectroChem*, vol. 1, no. 1, pp. 64–66, Jan. 2014.
- [29] J. Vila-Comamala, L. Romano, V. Guzenko, M. Kagias, M. Stampanoni, and K. Jefimovs, "Towards sub-micrometer high aspect ratio X-ray gratings by atomic layer deposition of iridium," *Microelectron. Eng.*, vol. 192, pp. 19–24, May 2018.
- [30] H. H. Tulskey, L. V. Liashek, H. S. Shevchenko, A. V. Vasilchenko, and O. A. Stelmakh, "Synthesis of functional nanocomposites based on aluminum oxide," *Funct. Mater.*, vol. 26, no. 4, pp. 718–722, 2019.
- [31] S. Xu and Y. Lei, "Template-assisted fabrication of nanostructured arrays for sensing applications," *ChemPlusChem*, vol. 83, no. 8, pp. 741–755, Aug. 2018.
- [32] V. V. Sysoeva, I. Kiselev, V. Trouillet, and M. Bruns, "Enhancing the gas selectivity of single-crystal SnO₂: Pt thin-film chemiresistor microarray by SiO₂ membrane coating," *Sens. Actuators B, Chem.*, vol. 185, pp. 59–69, Aug. 2013.
- [33] Q. Wang, J. Qiao, and S. Gao, "Fabrication of Zn_xIn_{1-x}S quantum dot-sensitized TiO₂ nanotube arrays and their photoelectrochemical properties," *Mater. Lett.*, vol. 131, pp. 354–357, Sep. 2014.
- [34] H. Haick, Y. Y. Broza, P. Mochalski, V. Ruzsanyi, and A. Amann, "Assessment, origin, and implementation of breath volatile cancer markers," *Chem. Soc. Rev.*, vol. 43, no. 5, pp. 1423–1449, 2014.
- [35] A. Amann, P. Mochalski, V. Ruzsanyi, Y. Y. Broza, and H. Haick, "Assessment of the exhalation kinetics of volatile cancer biomarkers based on their physicochemical properties," *J. Breath Res.*, vol. 8, no. 1, Feb. 2014, Art. no. 016003.
- [36] C. Deng, J. Zhang, X. Yu, W. Zhang, and X. Zhang, "Determination of acetone in human breath by gas chromatography–mass spectrometry and solid-phase microextraction with on-fiber derivatization," *J. Chromatography B*, vol. 810, no. 2, pp. 269–275, Oct. 2004.
- [37] J. Li, Y. Peng, and Y. Duan, "Diagnosis of breast cancer based on breath analysis: An emerging method," *Crit. Rev. Oncol./Hematol.*, vol. 87, no. 1, pp. 28–40, Jul. 2013.
- [38] C. Gessner *et al.*, "Exhaled breath condensate nitrite and its relation to tidal volume in acute lung injury," *Chest*, vol. 124, no. 3, pp. 1046–1052, Sep. 2003.
- [39] J. M. Piqué, M. Pallarés, E. Cusó, J. Vilar-Bonet, and M. A. Gassull, "Methane production and colon cancer," *Gastroenterology*, vol. 87, no. 3, pp. 601–605, Sep. 1984.
- [40] M. Phillips *et al.*, "Detection of lung cancer using weighted digital analysis of breath biomarkers," *Clinica Chim. Acta*, vol. 393, no. 2, pp. 76–84, Jul. 2008.
- [41] V. V. Sysoev *et al.*, "Single-nanobelt electronic nose: Engineering and tests of the simplest analytical element," *ACS Nano*, vol. 4, no. 8, pp. 4487–4494, Aug. 2010.
- [42] Y. Lin, Q. Lin, X. Liu, Y. Gao, and Z. Fan, "A controllable and widely applicable electrochemical anodization process to fabricate porous anodic aluminum oxide membrane," *Nanosc. Res. Lett.*, vol. 10, no. 1, pp. 1–8, 2015.